Petroleum Research 11 (2026) 935–948

Contents lists available at ScienceDirect

Petroleum Research

journal homepage: http://www.keaipublishing.com/en/journals/petroleum-research/

Full Length Article

Design and analysis of a micro hydraulic reamer-while-drilling tool

Xiaofeng Sun [a,b], Zuhai Qin [a,b,*], Wenhao Wang [a,b,**], Tie Yan [a,b]

[a] Key Laboratory of Enhanced Oil and Gas Recovery of Ministry of Education, Northeast Petroleum University, Daqing, 163318, China
[b] Sanya Offshore Oil & Gas Research Institute of Northeast Petroleum University, Sanya, 572025, China

ARTICLE INFO

Article history:
Received 15 May 2025
Received in revised form
19 January 2026
Accepted 20 January 2026
Available online 27 January 2026

Keywords:
Reamer-while-drilling (RWD)
Casing window sidetracking
Mature well remediation
Differential pressure tool
Slimhole drilling

ABSTRACT

Casing window sidetracking is a key technique for tapping remaining oil in small-scale enriched zones, such as minor anticlines and thin interbeds. While reaming-while-drilling (RWD) technology can mitigate issues like wellbore necking and stuck pipe caused by narrow sidetracked holes, conventional RWD tools are often excessively long, failing to meet the demands of high-curvature window sidetracking operations. To address this challenge, this study systematically investigates the structural principles and mechanical performance of hydraulic RWD tools. Through theoretical analysis, structural design, and numerical simulation, a novel micro hydraulic RWD tool activated by differential pressure was developed, followed by prototype fabrication and laboratory testing. The research results demonstrate that: Cutter stress analysis reveals that axial stress on arm is proportional to the cutting arc angle, while cutting resistance inversely correlates with it. An optimal 35° cutting arc angle minimizes resistance and prevents tool failure caused by locking ball bearing damage. The locking mechanism employs a line-line contact design between ball, housing, and sliding sleeve, effectively avoiding stress concentration and plastic strain. Based on hydrodynamic theory, the influence of the sliding sleeve's inner diameter on flow velocity, pressure differential, and total head loss was investigated, establishing a design methodology to ensure stable tool activation while minimizing energy dissipation. Applying thick-walled cylinder elastic theory, an interference-fit length calculation model was developed for the sleeve-housing interface. This methodology effectively prevents premature tool triggering while guaranteeing reliable arm retraction performance. Laboratory tests confirm successful tool activation/deactivation at theoretical flow rates, validating the design methodology. This study provides theoretical foundations for slimhole RWD tool design, enabling customized reaming applications. Its technical solutions hold significant economic and practical value for precisely exploiting residual reserves in mature wells and enhancing reservoir recovery efficiency.

© 2026 Chinese Petroleum Society. Publishing services by Elsevier B.V. on behalf of KeAi Communications Co. Ltd. This is an open access article under the CC BY license (http://creativecommons.org/licenses/by/4.0/).

1. Introduction

As the development of conventional shallow onshore oil and gas reservoirs enters the late production stage, the number of casing-damaged wells and shut-in wells continues to increase. Mature wells remediation and cost-performance optimization have become critical objectives in current oil and gas development (Lei et al., 2019; Zheng et al., 2022). Casing window sidetracking technology offers distinct advantages, including lower single-well costs, high target-zone accuracy, and reduced economic thresholds for recoverable residual oil volumes. This technique proves particularly effective for tapping small-scale residual oil accumulations in fault-block attic zones, narrow-angle structures, minor structural highs, and inter-well stagnant areas. As such, it serves as a vital technical approach for revitalizing low-productivity, shut-in, and abandoned wells in mature fields to improve ultimate recovery (Ismayilov and Mahmudov, 2024; Toczek and Wisniowski, 2024; Yuan et al., 2020; Zhang et al., 2019).

The casing window sidetracking operation in production casing is constrained by the original wellbore size, resulting in a smaller sidetracked hole and narrow annular clearance. Taking typical field drilling dimensions as examples: for a 7-inch casing sidetrack with

* Corresponding author. Key Laboratory of Enhanced Oil and Gas Recovery of Ministry of Education, Northeast Petroleum University, Daqing, 163318, China.
** Corresponding author. Key Laboratory of Enhanced Oil and Gas Recovery of Ministry of Education, Northeast Petroleum University, Daqing, 163318, China.
E-mail addresses: QZH420527@126.com (Z. Qin), wwh0824@foxmail.com (W. Wang).

Peer review under the responsibility of Editorial Office of Petroleum Research.

https://doi.org/10.1016/j.ptlrs.2026.01.011
2096-2495/© 2026 Chinese Petroleum Society. Publishing services by Elsevier B.V. on behalf of KeAi Communications Co. Ltd. This is an open access article under the CC BY license (http://creativecommons.org/licenses/by/4.0/).

a 152.4 mm borehole, the clearance between the 127 mm tailpipe (142 mm coupling) and wellbore is merely 5–12 mm; while for a 5½-inch casing sidetrack with 118 mm borehole, the 102 mm tailpipe (110 mm coupling) maintains only 4–8 mm clearance, which is further reduced by mud cake presence. With existing well deviation and difficulty in installing centralizers, the casing tends to contact the borehole wall, leading to cement channeling or incomplete filling. This results in thin, poor-quality cement sheaths that are prone to damage during subsequent operations, causing common issues like water channeling and casing failure, ultimately compromising cementing quality and wellbore longevity (Noviasta et al., 2017). To address these challenges, extensive research has been conducted by domestic and international scholars focusing on cement slurry rheology mechanisms, novel cement systems, and cementing process optimization. However, improvement outcomes remain limited. Studies demonstrate that even advanced cementing materials and technologies struggle to perform effectively within such constrained annular spaces. Recent years have witnessed growing industry acceptance of hole-enlargement technology as an effective solution to transform slimhole cementing into conventional cementing by increasing annular clearance. Studies reveal that expanding the cement sheath thickness to 20–25 mm can substantially mitigate damage during various well operations including steam injection, perforation, workover and production. This approach fully capitalizes on established cementing technologies to improve cementing quality and preserve production casings, ultimately emerging as the optimal technical solution for ensuring well integrity while enhancing operational safety and efficiency in oil and gas wells (Shokry et al., 2021; Toczek et al., 2023; Zhao and Liao, 2021).

The primary hole-enlargement techniques consist of post-drilling reaming and reaming-while-drilling (RWD). Leading oilfield service companies, including DIAMANT, have developed fixed-arm hole enlarging tools that are categorized into split-type and integral-type configurations. These tools feature a robust structural design comprising a cylindrical body, expandable arms, nozzles, cutting elements, and arm-protecting alloy posts, demonstrating exceptional tensile/torsional resistance and operational reliability. The optimized wear-resistant surface treatment further enhances their service life while mitigating sticking risks. However, its fixed structural dimensions make it difficult to meet the requirements for internal hole enlargement in existing wellbores, rendering post-drilling reaming methods inapplicable. The RWD technology emerges as a technically viable alternative, enabling borehole enlargement in a single trip to achieve economic efficiency. This approach holds significant technical value for optimizing well architecture, mitigating wellbore narrowing in plastic formations, and enhancing overall drilling efficiency (Li et al., 2023; Murillo et al., 2018; Weng et al., 2025).

Most mainstream RWD tools currently employ a sliding hydraulic expansion mechanism, which demonstrates superior operational reliability and drilling efficiency. Based on activation methods, they are primarily categorized into ball-drop activation, pressure differential activation, and radio-frequency identification (RFID) activation. These tools are widely applicable to conventional drilling, window sidetracking, casing drilling, and multilateral well construction (Liu et al., 2022; Zhang et al., 2024). Leading service companies have developed multiple generations of hydraulic expandable RWD tools that have successfully addressed complex drilling challenges. Ball-drop activated systems dominate current deployments, with Halliburton's XR™ reamer (Mancini et al., 2009) setting industry benchmarks through its 1.5x hole enlargement ratio, full-flow circulation capability during tripping operations, and vibration-dampening design that ensures stable reaming performance. Schlumberger's Rhino series (Torvestad et al., 2012) reamers incorporate a reliable dual-ball locking/unlocking mechanism with demonstrated reliability in field operations. The tool's unique directional capability during mud circulation enables effective deployment in extended-reach drilling (ERD) applications, highly abrasive formations, and cyclically stressed expanding formations requiring full-bore activation. Baker Hughes' GaugePro series reamers (XPR and upgraded XPS models) (Vila et al., 2011), incorporate a unique activation mechanism that operates independently of weight-on-bit (WOB), flow rate, or bottomhole assembly (BHA) pressure, effectively eliminating risks of premature triggering. The simplified design employs minimal components while excluding complex mechanical systems, thereby enhancing operational reliability and reducing downhole failure potential. These tools maintain full compatibility with all standard measurement-while-drilling (MWD)/logging-while-drilling (LWD) systems, rotary steerable systems (RSS), and high-performance drilling motors, making them particularly suitable for demanding applications where tool reliability is paramount (Al-Essa, 2015). The pressure-differential activated tool represented by Nabors Industries' TESCO Underreamer (Morel et al., 2010) features robust arm structures with fixed-cutter PDC designs, enabling higher weight-on-bit (WOB) to enhance rate of penetration (ROP). Its heavy-duty rack-and-pinion system ensures complete arm deployment and reliable retraction. Weatherford's RipTide reamer (Loreto et al., 2022) represents the RFID-enabled downhole tools, utilizing wireless radio-frequency identification technology to allow virtually unlimited activation/deactivation cycles during both tripping and drilling operations. This system incorporates advanced downhole sensors that monitor and record critical wellbore parameters including triaxial vibration, annular pressure, and formation temperature, providing operators with diagnostic capabilities for enhanced decision-making (Snider and Fraley, 2007; Valverde, 2018).

Existing reamer models exhibit significant limitations, including excessive length and oversized body diameter, which reduce drill string flexibility and hinder directional sidetracking capability. These constraints make conventional reamers unsuitable for slimhole well window sidetracking operations in mature wellbores. To address the high-curvature challenges in slimhole window sidetracking operations, this study designed a compact hydraulic RWD tool with 120 mm diameter and 900 mm length, specifically tailored for a certain oilfield conditions. The design incorporated optimized arm cutting arc geometry, a reliable locking mechanism, and hydraulically tuned sleeve inner diameter (Zhu et al., 2023). Guided by theoretical computational data, the reamer prototype was fabricated and subsequently subjected to laboratory testing to validate its operational performance. This research provides a technical solution to optimize reserve recovery efficiency, and improve oil and gas production rates in mature oilfields.

2. Structural design

The micro hydraulic reamer-while-drilling (RWD) tool utilizes a differential pressure activation mechanism to control the deployment and retraction of reamer arm. By performing post-drill reaming, it enlarges the annular clearance and increases the cement ring thickness, thereby enhancing cementing quality without relying on new materials or technologies of limited effectiveness. A locking mechanism ensures wellbore gauge maintenance after drilling, guaranteeing wellbore quality. By adjusting mud flow rates, the tool enables flexible control of repeated arms activation/retraction during different well sections or operational phases, allowing seamless transition between

reaming and non-reaming drilling modes. This functionality significantly reduces non-productive tripping time while improving drilling efficiency and lowering operational costs. As shown in Fig. 1, the tool's main components include: sliding sleeve, housings, reamer arms, locking ball, washpipe, seal stacks, and return spring.

During conventional drilling, the reamer arms remain retracted within the housings, with the locking ball stationary at the bottom of the W-shaped track on the outer sleeve (Fig. 2a). When entering the reaming section, increasing the mud flow rate drives the sliding sleeve downward under annular pressure, compressing the return spring. The ball travels along the W-shaped track on the outer surface of the sleeve while maintaining a constant axial position within the annular groove on the inner wall of the housing (Fig. 2d), until reaching a state of force equilibrium at the top of the track (Fig. 2b), thereby initiating the radial deployment of the cutter arms. Upon flow cessation and pressure release, the sleeve is lifted upward by the restoring force of the spring. The ball continues to move along the annular groove on the inner wall of the housing (Fig. 2d) until a force equilibrium is reestablished at the sub-top of the track (Fig. 2c), at which point the cutter arms are fully deployed and locked, completing the activation of the reamer. Post-reaming, resuming high flow disengages the ball from the locked position. Subsequent pressure release enables sleeve retraction via spring force, resetting the ball to the track bottom (Fig. 2a) and retracting the arms, concluding the reaming cycle.

3. Design and optimization of critical components

3.1. Reamer arm cutting structure optimization

As shown in Fig. 3, a Cartesian coordinate system is established with the central point O of the three-arm top as the origin, defining radial and axial axes. The total number of cutters on the reamer arms is denoted as N_x, with each cutter center characterized by coordinates (R_c, H_c, θ_c), normal angle γ_c, back rake angle α, and side rake angle β. Here, R_c represents the radial coordinate (distance from the cutter's center point to the central axis when fully expanded), H_c indicates the axial coordinate (axial distance from the cutter center to origin O), and θ_c defines the circumferential angle (measured from the arm' 0° reference line). Given the minimal curvature of the cutting section, its profile is simplified as a linear segment forming angle λ (cutting arc angle) with the axial direction, where λ and γ_c are complementary angles. The resultant force on each cutter is decomposed into three orthogonal components: axial force F_v, tangential cutting force F_c, and radial forces F_r/F_{rr}. The tangential component (F_c) represents the primary cutting force, while axial force and radial forces are calculated as:

$$F_v = F_n \sin\lambda$$

$$F_r = F_n \cos\lambda$$

$$F_{rr} = F_c \tan\beta \quad (1)$$

The reamer arm is divided into three functional sections: the cutting section (lower), gauge-holding section (middle), and back-reaming section (upper). The cutting section serves as the primary borehole enlargement zone. This study focuses on optimizing the cutting section profile to reduce both cutting resistance and upward axial force transmission while maintaining required hole enlargement performance.

To address the hard and interbedded formations in the target oilfield, the cutting section adopts an impact-resistant large-curvature arc profile (Fig. 4), with defined geometric parameters: fully deployed height (H), maximum radius (R_1), and crown radius (R_0), $\lambda = \arctan\frac{R_1-R_0}{H}$.

To investigate the influence of the cutting arc angle (λ) on the transmission of axial and radial forces, boundary conditions were applied to the reamer arm as illustrated in Fig. 5. The base of the reamer arm was fixed to simulate the locked cutting state. Under a weight-on-bit (WOB) condition of 10 kN, the load was applied as normal pressure on the surface of a single cutter. Based on the field-grade reamer arm structure, four angles (15°, 25°, 35°, 45°) were selected for mechanical simulation analysis (Fu et al., 2022; Koulidis et al., 2022).

Simulation parameters were set according to field tool materials and drilling conditions: the arm was made of 42CrMo steel with an elastic modulus of 212 GPa, a Poisson's ratio of 0.3, and a yield strength of 930 MPa; the cutter was composed of PDC material with an elastic modulus of 910 GPa, a Poisson's ratio of 0.07, exhibiting extremely high hardness and wear resistance. A refined hexahedron-dominant mesh with a minimum element size of 0.1 mm was applied in the force-bearing region of the PDC cutter, while a coarser mesh was used in other areas to ensure computational accuracy and efficiency. The simulation results are shown in Figs. 6 and 7.

The stress contour plots reveal hat as λ increases from 15° to 45°, the axial stress exhibits a 73.5% enhancement while the radial stress demonstrates a 21% reduction, indicating significantly higher sensitivity of axial stress to λ variations compared to radial stress. Further data processing yielded stress variation curves (Fig. 8), showing that axial stress on the arm increases while radial stress decreases with larger λ. To prevent locking ball damage, reducing λ is necessary to decrease axial reaction forces during rock breaking.

A model for estimating the cutting resistance of the reamer arm is established, incorporating the cutting resistance (F), the cutting area (A), the contact arc length (S), the cutting arc angle (λ), and the rock drillability (K).

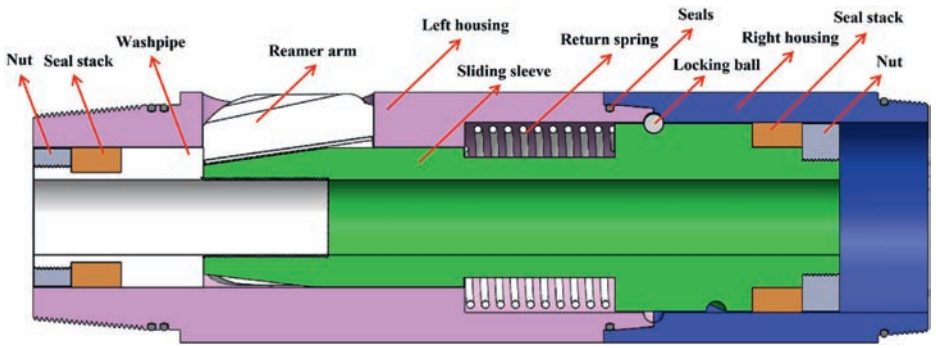


Fig. 1. Micro hydraulic RWD tool schematic.

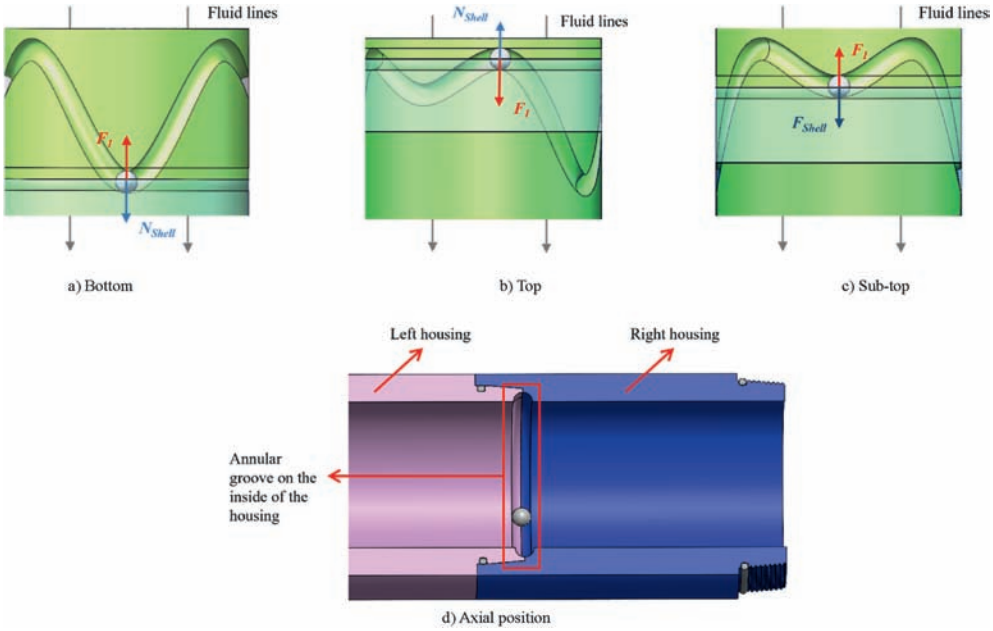


Fig. 2. Activation mechanism schematic: Locking ball position and force analysis.

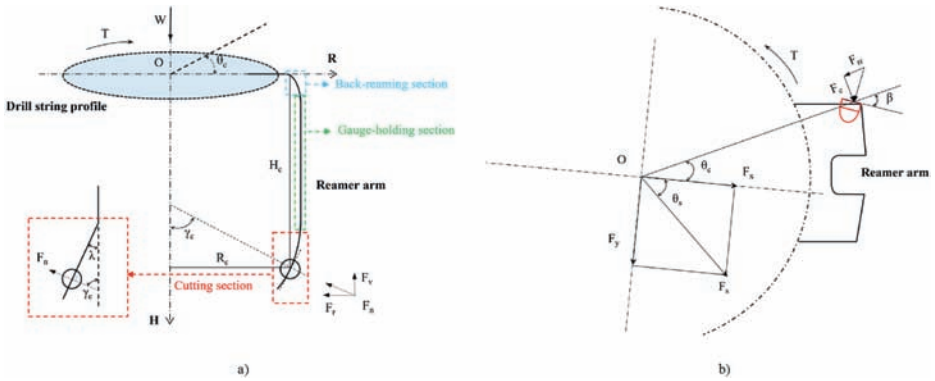


Fig. 3. Schematic of cutter orientation and force analysis for reamer arm.

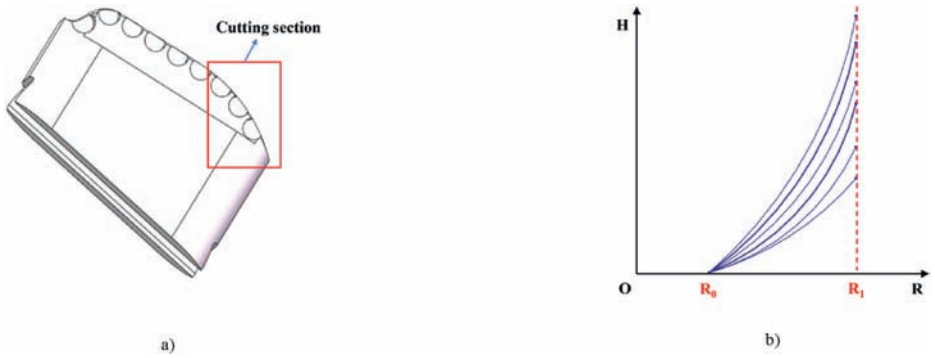


Fig. 4. Geometric schematic of cutting section.

$$\begin{cases} F = \lambda AS + b \\ \lambda = \left(0.001\lambda^2 - 0.012\lambda + 0.483\right)K^2 \\ b = \left(0.025\lambda^2 - 0.36\lambda + 22.985\right)K^2 \end{cases} \quad (2)$$

Under the condition of a constant cutter arm radius, reducing λ increases the arc length of the cutting section, thereby extending the S. Taking $K = 3$ as an example, the variation trend of cutting resistance under different λ was analyzed. The results are shown in Fig. 9. The relationship between F and λ follows a logarithmic function curve. Both excessively large and small values of λ result

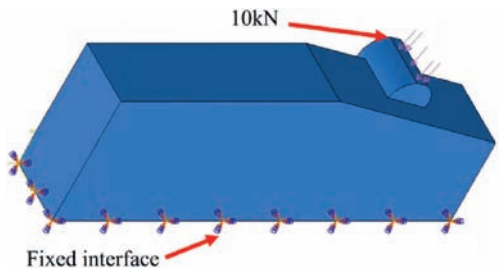


Fig. 5. Schematic of boundary conditions for mechanical simulation of reamer arm.

in an increase in F, which is detrimental to reaming operations (Doshvarpassand et al., 2017; Rostamsowlat et al., 2018). Considering these factors comprehensively, λ is optimally selected as 35°.

3.2. Force analysis and optimization of locking mechanism

The locking ball plays a critical role in the locking mechanism, and its force analysis is essential for the mechanism's design and optimization. Fig. 10 illustrates the force analysis of the ball during the reamer's operation. The ball's gravity is negligible compared to the WOB, and the ball maintains equilibrium under three primary forces: the radial (F_1) and axial (F_2) forces exerted by the housing, and the normal force (F_3) applied by the sliding sleeve.

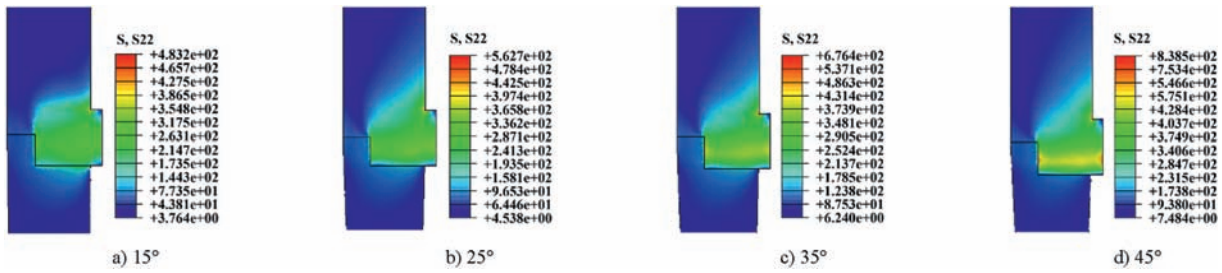


Fig. 6. Axial stress contour plot of reamer arm.

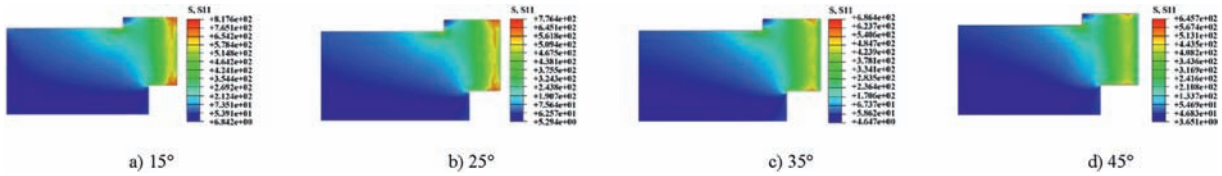


Fig. 7. Radial stress contour plot of reamer arm.

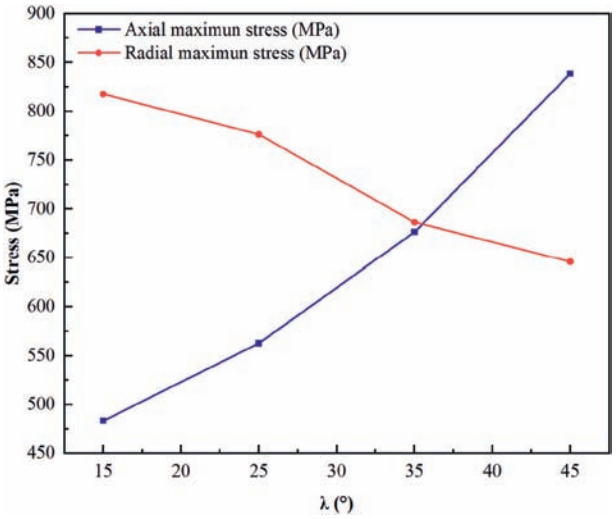


Fig. 8. λ-Dependent maximum stress trend.

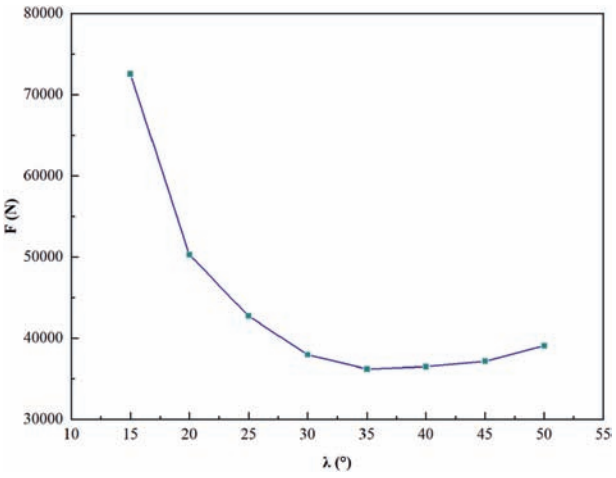


Fig. 9. The variation trend of F with λ.

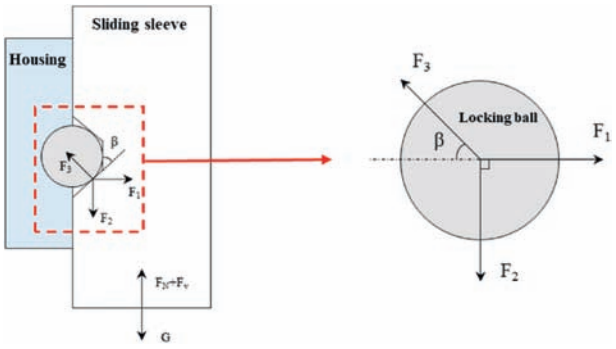


Fig. 10. Locking ball force analysis.

This study investigates the pressure-bearing characteristics of the locking mechanism during drilling operations through mechanical simulations of various design configurations. The selection of tool materials and drilling parameters was based on field applications. The housing and sliding sleeve were made of 42CrMo (yield strength ≥930 MPa), while the locking ball was manufactured from G55SiMoVA (yield strength ≥1850 MPa), which exhibits high hardness and high yield strength, with an elastic modulus of 210 GPa, a Poisson's ratio of 0.29, and a density of 7.85 g/cm^3.In the critical contact regions between the locking ball, sliding sleeve, and housing, as well as in areas with stress concentrations such as flat surfaces and grooves, a high-precision hexahedron-dominant mesh was employed, with a minimum element size of 0.2 mm. Other non-critical regions utilized a coarser mesh to reduce computational cost. Mesh quality was rigorously controlled, ensuring a Jacobian ratio greater than 0.7 and an element aspect ratio below 5.

The boundary conditions were set as shown in Fig. 11. The distal end face of the housing was fully fixed. Radial displacement of the outer surface of the sliding sleeve was constrained, allowing only axial movement to simulate its constrained state within the drill string. An axial force of 10 kN was applied to the reference point at the bottom end of the sliding sleeve to simulate the WOB load during the drilling process. All contact pairs were defined as surface-to-surface contact.

Stress analysis conducted in accordance with Alloy structure steels (GB/T 3077-2015) (SAMR and NSA, 2015) and High-carbon chromium bearing steel (GB/T 18254-2016) (SAMR and NSA, 2016) standards guided design optimizations to maintain all stress values within safe operational limits.

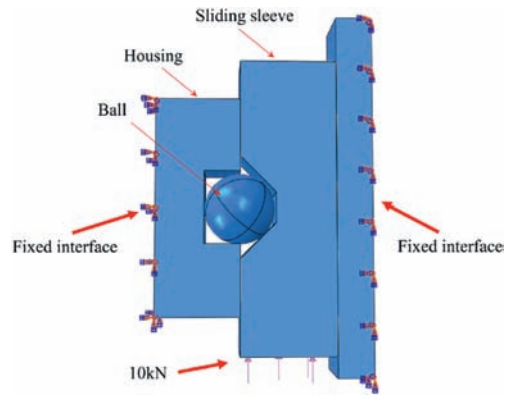


Fig. 11. Schematic diagram of boundary conditions for mechanical simulation of the locking mechanism.

(1) Initial mechanism stress-strain analysis

Figs. 12 and 13 present the stress and strain contour plots of the locking ball, sliding sleeve, and housing. The stress distribution at the point-line contact interfaces exhibits a flattened band pattern, with concentrated force zones observed on the ball in both design configurations. Comparative analysis of stress/strain contours reveals the point-line contact configuration reduces peak stress by 2.6% and maximum strain by 78.6% versus conventional point-point contact. Component-specific stress reductions reach 28.1% (housing) and 1.2% (sliding sleeve), demonstrating particularly significant mitigation of locking ball strain localization and housing stress concentration.

Table 1 summarizes the maximum stress and strain data for each component from Figs. 12 and 13. Under point-line contact conditions, the housing exhibited a peak stress of 677 MPa, while both the housing and sliding sleeve exceeded the yield strength of 42CrMo (930 MPa) in other configurations. The locking ball's maximum stress surpassed the yield strength of G55SiMoVA (1850 MPa), resulting in plastic strain. The point-contact regions demonstrate higher stress concentrations than line-contact regions. The point-point contact configuration induces significant ball deformation, potentially causing mechanical interference that may prevent proper reamer activation/deactivation. Neither configuration meets the design specifications.

(2) Optimized mechanism stress-strain analysis

Building upon the initial mechanism design, the ball-sleeve contact interface was optimized to a line-line contact geometry, the simulation results are shown in Fig. 14. Stress/strain analysis indicates peak stresses of 741.2 MPa (housing), 658.2 MPa (sliding sleeve), and 1187 MPa (locking ball), all substantially below their respective yield strengths. The ball's maximum strain (0.025 mm) remains within design tolerance thresholds.

Table 2 compares the mechanical results of three design configurations. The line-line contact configuration demonstrates significant improvements, reducing maximum component stresses by 24%–38% and ball strain by 88% compared to point-point contact, with all parameters remaining within acceptable operational limits. This optimized design achieves more uniform load distribution in the locking mechanism, effectively preventing plastic strain induced by stress concentration. The refined line-line contact configuration significantly enhances the mechanical performance of the locking mechanism, fulfilling operational requirements while reliably maintaining all critical functions including tool activation, deactivation, and positive locking.

3.3. Sliding sleeve inner diameter design

The drilling fluid flows through the sliding sleeve's internal cavity, where the inner diameter serves as the critical parameter governing throttling pressure drop. As modeled in Fig. 15, key geometric and flow parameters include: the sleeve/washpipe interior length (L), inner diameter (d_0), flow area (S_0), and velocity (v_0); the upper pressure buildup annulus diameter (d_1), cross-sectional area (S_1), and velocity (v_1); and the lower flow channel diameter (d_1), area (S_1), and velocity (v_1).

The drilling fluid experiences three primary head loss components as it flows from the pressure buildup annulus through the sleeve/washpipe assembly into the lower flow channel: Local head

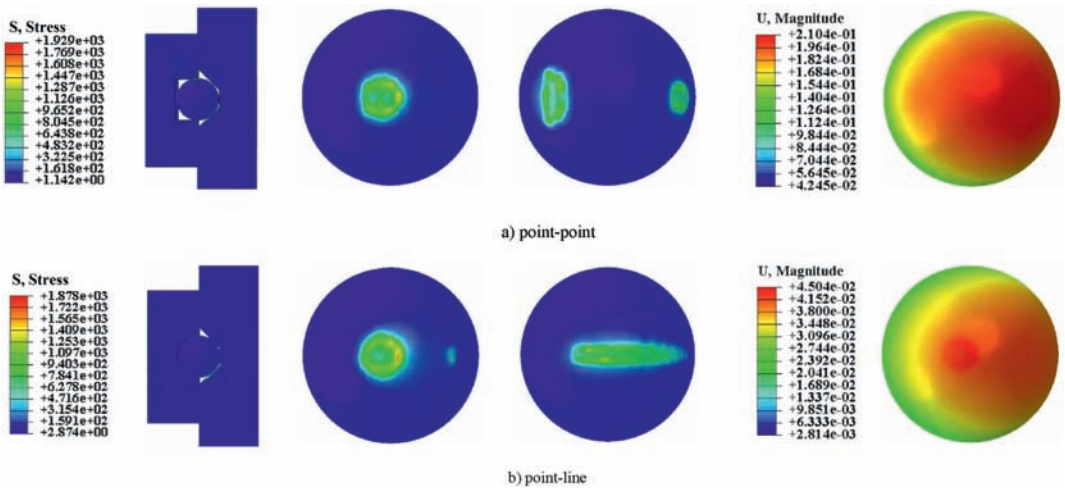


Fig. 12. Locking ball stress/strain contour plots.

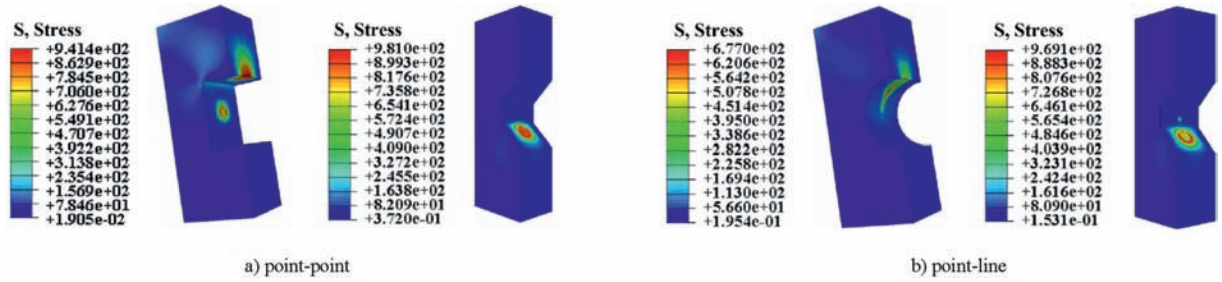


Fig. 13. Sliding sleeve and housing stress contour plots.

Table 1
Maximum stress and strain of prototype design components.

	point-point		point-line	
	Max stress (MPa)	Max strain (mm)	Max stress (MPa)	Max strain (mm)
Housing	941	/	677	/
Sliding sleeve	981	/	969	/
Locking ball	1929	0.210	1878	0.045

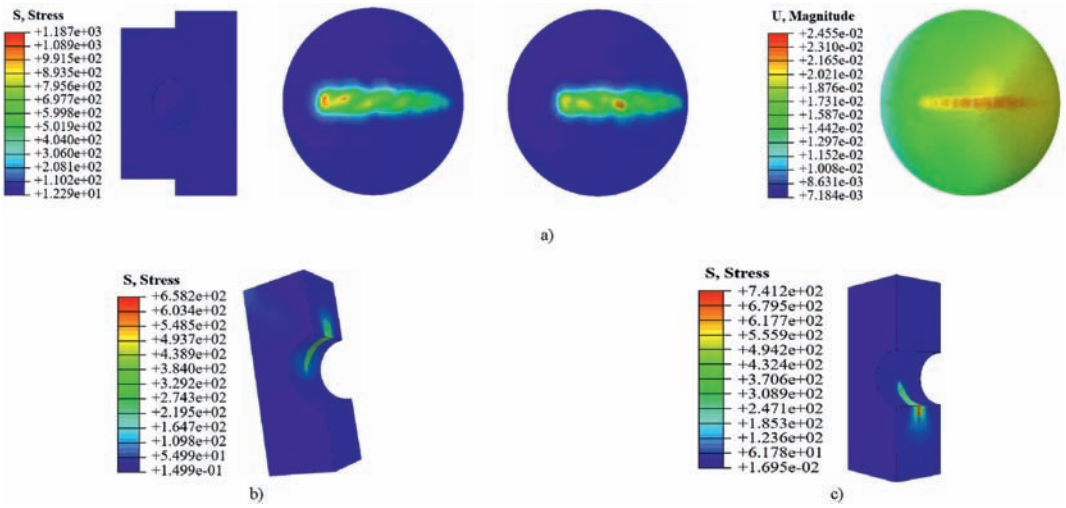


Fig. 14. Stress and strain contour plots under line-line contact configuration.

Table 2
Maximum stress and strain under different contact configurations.

	Max stress (MPa)			Max strain (mm)		
	point-point	point-line	line-line	point-point	point-line	line-line
Housing	941	677	658	/	/	/
Sliding sleeve	981	969	741	/	/	/
Locking ball	1929	1878	1187	0.210	0.045	0.025

loss from sudden flow area contraction (A_1), frictional head loss along the sleeve/washpipe interior, and local head loss from sudden flow area expansion at the washpipe outlet (A_2). For $d_0 \in [30,70]$ mm, the Reynolds number of drilling fluid flow through the sleeve and washpipe internal cavity was calculated, with the internal surface roughness values corresponding to standard steel pipes ($\Delta = 0.19mm$). According to engineering fluid mechanics, the expression for calculating the Reynolds number (Re) of fluid in a pipeline is as follows:

$$\mathrm{Re} = \frac{\rho v d}{\mu} \tag{3}$$

where ρ is the drilling fluid density (g/cm^3); v is the drilling fluid velocity (m/s); d is the pipe diameter (m); μ is the dynamic viscosity of the drilling fluid (mPa·s). If $Re < 2000$, the flow regime of the drilling fluid is laminar; otherwise, it is turbulent.

The Bernoulli equation is applied between cross-sections A_1 and A_2 (reference plane) as follows:

$$z_1 + \frac{p_1}{\rho g} + \frac{{v_1}^2}{2g} = z_2 + \frac{p_2}{\rho g} + \frac{{v_2}^2}{2g} + h_w \tag{4}$$

where z_1 and z_2 denote the elevation heads at A_1 and A_2 respectively (m), p_1 and p_2 represent the pressures at A_1 and A_2 respectively (Pa), v_1 and v_2 indicate the flow velocities in the upper pressure buildup annulus and lower flow channel respectively (m/s), and h_w signifies the total head loss between A_1 and A_2 (m), with the elevation difference ($\Delta z = z_2 - z_1$) being negligible compared to other hydraulic terms.

The pressure difference (Δp) generated between cross-sections A_1 and A_2 is calculated as:

$$\Delta p = p_1 - p_2 = \left(\frac{{v_2}^2 - {v_1}^2}{2g} + h_w + z_2 - z_1\right)\rho g \tag{5}$$

The total head loss (h_w) is expressed as:

$$h_w = \delta_1 \frac{{v_1}^2}{2g} + \delta_0 \frac{{v_0}^2}{2g} + \delta_2 \frac{{v_2}^2}{2g} \tag{6}$$

Based on field drilling data (drilling fluid: μ = 10 mPa s, ρ = 1.6 g/cm^3) and the target well section's operating flow rate (16 L/s), the tool activation flow rate is set at 30 L/s to exceed normal operational requirements, consistent with the micro-reamer's working principle. The design specifies the pressure buildup annulus diameter ($d_1 = 85$ mm), lower washpipe channel diameter ($d_2 = 77$ mm), and sleeve-washpipe interior total length ($L = 814$ mm). According to Eq. (3), the Reynolds number (Re) for the pressure-trapped annulus above the sliding sleeve is calculated to be 71,937, while that for the lower flow channel is 79,411. Furthermore, when the inner diameter of the sliding sleeve (d_0) varies within the range of 30 mm–70 mm, all calculated Re exceed 2000, as shown in Fig. 16. This indicates that the fluid remains in a turbulent flow regime across this parameter range.

Within the defined range of sleeve inner diameters ($d_0 \in [30,70]$ mm), this investigation establishes the functional relationships between d_0 and three key hydraulic parameters: the flow velocity (v_0), pressure differential (Δp), and total head loss (h_w). As illustrated in Fig. 17, the characteristic curves approximate logarithmic functions: The [30,40] mm interval exhibits drastic fluctuations in Δp (1.78 MPa decrease) and h_w (113.43 m reduction), transitioning to moderated declines of 0.38 MPa and 23.9 m respectively in the [40,50] mm range, before stabilizing with negligible variations of 0.14 MPa and 8.71 m in the [50,70] mm domain. Flow velocity (v_0) demonstrates mean fluctuations of 2 m/s for $d_0 \in [30,50]$ mm, diminishing to under 0.3 m/s in the [50,70] mm range.

To ensure mild fluctuations of all three parameters, the range of d_0 was determined to be 50–70 mm. Given the inverse relationship between the inner diameter of the sliding sleeve and its wall thickness (the wall thickness decreases as the inner diameter increases), and considering the significant influence of wall thickness on the torsional performance of the sleeve, the mechanical behavior under the minimum wall thickness condition was emphasized. The sleeve model was appropriately simplified and assigned the material 42CrMo. A predominantly hexahedral mesh was applied with a minimum element size of 0.2 mm. The top end face was fully fixed, and the outer surface was constrained in the

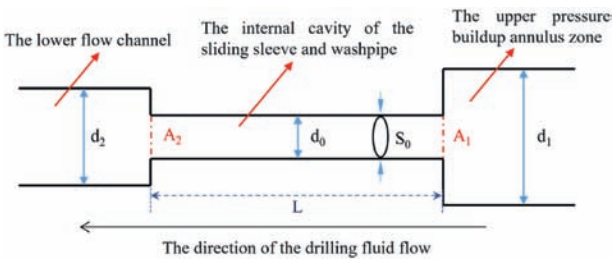


Fig. 15. Throttling model at sliding sleeve diameter transition zone.

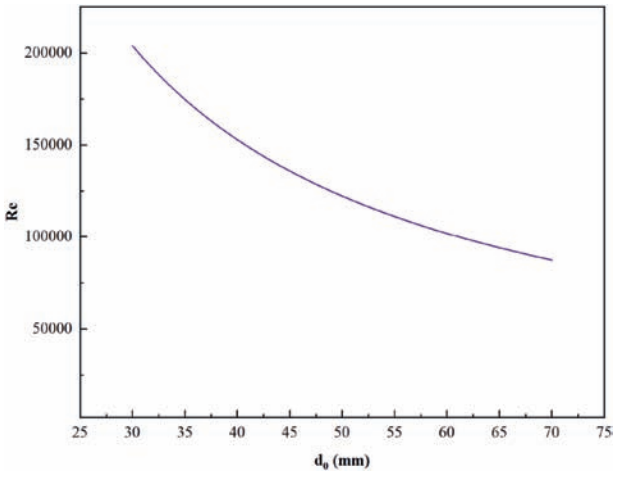


Fig. 16. Re corresponding to different d_0 of the sliding sleeve.

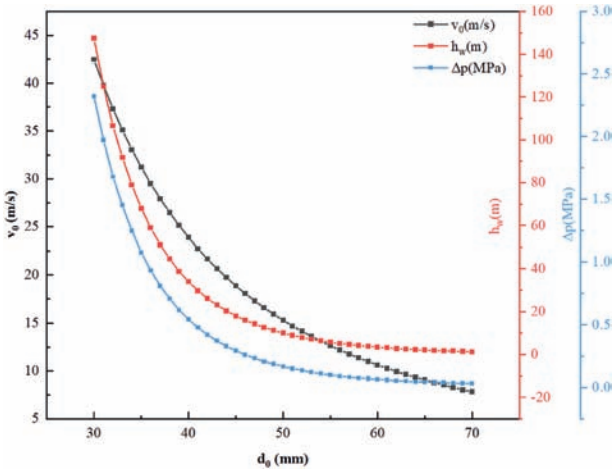


Fig. 17. Functional relationships among d_0, v_0, and h_w.

axial direction. A torque load of 30 kN m was applied to simulate the ultimate torsional capacity. The results are shown in Fig. 18.

According to the stress contour, the maximum stress of the sleeve under the condition of $d_0 = 50$ mm is 921.6 MPa, which remains below the yield strength limit of 42CrMo (930 MPa), thus satisfying the strength requirement. In contrast, all other inner diameter values result in stress levels that exceed the allowable safety margin. Furthermore, the axial thrust actuating the sleeve during operation is composed of the combined hydraulic force and the return spring force, while also needing to overcome the friction between the sleeve and the inner wall of the housing. Therefore, the pressure-bearing area of the sleeve should not be too small. Considering both structural safety and operational reliability, an inner diameter of $d_0 = 50$ mm was ultimately selected.

3.4. Interference length design for sliding sleeve-housing interface

The design of the interference fit between the sliding sleeve and housing requires precise calibration to satisfy two critical operational requirements. Under normal flow conditions, the generated annular pressure must be insufficient to overcome the static friction and initiate sleeve movement. Conversely, at predetermined activation flow rates, the hydraulic thrust must adequately exceed the combined resistance from both sleeve-housing friction and return spring restoring force to ensure reliable sleeve displacement and subsequent arm expansion. Notably, the frictional contribution from packing elements can be safely disregarded under downhole high-pressure environments.

The return spring, manufactured from hot-rolled spring steel (shear modulus = 78 GPa), demonstrates a pre-activation restoring force of 16,544 N, reaching its maximum designed load of 41,362 N at complete arm deployment. Taking cross-section A_1 as the reference plane, the Bernoulli equation is formulated between this reference plane (A_1) and the mud pump discharge section (A_3) as follows:

$$z_3 + \frac{p_3}{\rho g} + \frac{{v_3}^2}{2g} = z_1 + \frac{p_1}{\rho g} + \frac{{v_1}^2}{2g} + h_f \tag{7}$$

where z_3 denotes the elevation head at section A_3 (m), p_3 represents the pressure at A_3 (Pa), v_3 indicates the drilling fluid flow velocity at A_3 (m/s), and h_f corresponds to the frictional head loss (m). $\frac{{v_3}^2}{2g} - \frac{{v_1}^2}{2g}$ is negligible compared to other terms in the equation.

Combining Eq. (4) and Eq. (6), the axial momentum conservation equation for the sleeve inlet (A_1) and washpipe outlet (A_2) is formulated as:

$$p_1 S_{10} - p_2 S_{20} - F = \rho Q(v_2 - v_1) \tag{8}$$

where S_{10} and S_{20} denote the cross-sectional areas at the sleeve inlet and washpipe outlet, respectively (m^2), and F represents the hydraulic force exerted by the drilling fluid on the sleeve inlet (N).

The sleeve was designed with an inner diameter of 50 mm. Based on Eq. (8), the relationship between drilling fluid flow rate (Q) and the resultant thrust force (F) on the sleeve was established, as illustrated in Fig. 18. This demonstrates that the thrust force acting on the sleeve can be controlled by adjusting the drilling fluid flow rate.

As shown in Fig. 19, F shows a positive correlation with Q, when $d_0 = 50$ mm and $Q = 16$ L/s, $F = 27{,}841$ N with a return spring force of 16,544 N. The friction between the sleeve and housing must exceed the resultant force (11,297 N) to prevent premature reamer activation. At $Q = 30$ L/s, $F = 55{,}403$ N with a maximum spring force of 41,362 N, requiring F to overcome the combined friction and spring force (14,041 N) for activation. Meanwhile, friction must remain below the minimum spring force (16,544 N) to

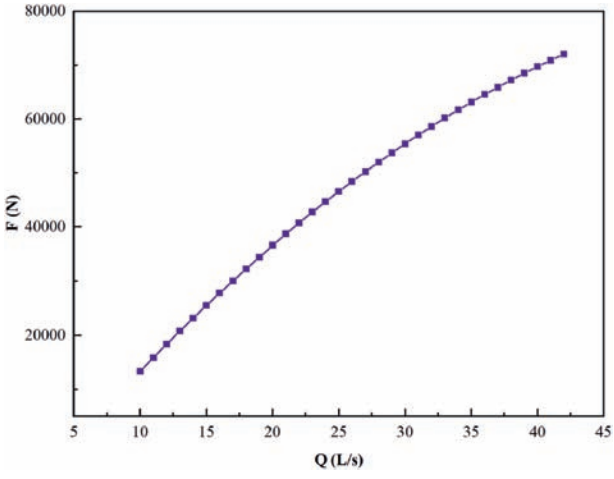


Fig. 19. Relationship between F and Q.

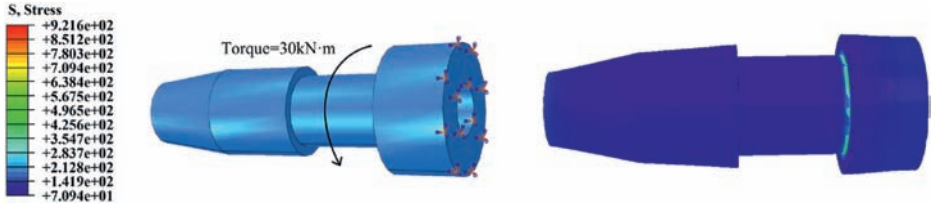


Fig. 18. Boundary condition and stress contour of the sleeve under ultimate torque simulation at $d_0 = 50$ mm.

ensure arm retraction. Therefore, the sleeve-housing friction should be maintained between 11,297 N and 14,041 N. The frictional force between the sleeve and housing with an interference fit is calculated by:

$$F_f = \mu F_N = \mu p S = 2\pi R h \mu p \tag{9}$$

where F_f denotes the frictional force between the sleeve and housing (N), μ represents the coefficient of friction, p signifies the contact pressure at the sleeve-housing interface (MPa), S corresponds to the nominal contact area (mm^2), h indicates the axial length of the interference fit region (mm), and R is the outer radius of the sleeve (mm).

This study employs the thick-walled cylinder elasticity theory from elastic mechanics to analyze the relationship between the interference fit magnitude (δ) and contact pressure (p). According to elastic theory, the radial displacement at any point within a thick-walled cylinder subjected solely to internal pressure is given by:

$$u = \frac{1}{E}\frac{a^2 p_i}{b^2 - a^2}\left[(1+\varphi)\frac{b^2}{r} + (1-\varphi)r\right] \tag{10}$$

where u represents the displacement component at any point (mm), p_i denotes the internal pressure acting on the cylinder (MPa), r indicates the radial coordinate of the point (mm), a and b correspond to the inner and outer radius of the cylinder respectively (mm), E signifies the elastic modulus of the material (GPa), and φ represents Poisson's ratio of the cylinder material.

For a thick-walled cylinder subjected solely to external pressure, the radial displacement at any point within the cylinder wall is given by:

$$u = -\frac{1}{E}\frac{b^2 p_o}{b^2 - a^2}\left[(1+\varphi)\frac{a^2}{r} + (1-\varphi)r\right] \tag{11}$$

where p_0 represents the external pressure acting on the cylinder (MPa).

The relationship between the interference (δ) and contact pressure (p) can be determined using Eq. (10) and Eq. (11). After assembly of the housing and sleeve, the total interference is δ, where the housing with outer radius R_c and inner radius R_b expands radially by δ_1 at the inner surface, while the sleeve with inner diameter R_a contracts radially by δ_2 at the outer surface (as illustrated in Fig. 20).

Following assembly, the contact pressure (p) develops at the sleeve-housing interface. For the housing, this pressure acts as an internal load, generating radial displacement (δ_1) at the bore surface. From Eq. (10), this relationship is expressed as:

$$\begin{aligned}\delta_1 &= \frac{1}{E}\frac{{R_b}^2 p}{{R_c}^2 - {R_b}^2}\left[(1+\varphi)\frac{{R_c}^2}{R_b} + (1-\varphi)R_b\right] \\ &= \frac{R_b p\left[\varphi\left({R_c}^2 - {R_b}^2\right) + {R_c}^2 + {R_b}^2\right]}{E\left({R_c}^2 - {R_b}^2\right)}\end{aligned} \tag{12}$$

The assembled sleeve experiences the contact pressure (p) as an external load, resulting in radial displacement (δ_2) at its outer diameter. From Eq. (11), this relationship is expressed as:

$$\begin{aligned}\delta_2 &= -\frac{1}{E}\frac{{R_b}^2 p}{{R_b}^2 - {R_a}^2}\left[(1+\varphi)\frac{{R_a}^2}{R_b} + (1-\varphi)R_b\right] \\ &= \frac{R_b p\left[\varphi\left({R_a}^2 - {R_b}^2\right) + {R_a}^2 + {R_b}^2\right]}{E\left({R_b}^2 - {R_a}^2\right)}\end{aligned} \tag{13}$$

Total interference δ equals the sum of displacements:

$$\begin{aligned}\delta = &\frac{R_b p\left[\varphi\left({R_c}^2 - {R_b}^2\right) + {R_c}^2 + {R_b}^2\right]}{E\left({R_c}^2 - {R_b}^2\right)} \\ &+ \frac{R_b p\left[\varphi\left({R_a}^2 - {R_b}^2\right) + {R_a}^2 + {R_b}^2\right]}{E\left({R_b}^2 - {R_a}^2\right)}\end{aligned} \tag{14}$$

The contact pressure (p) is obtained as:

$$p = \frac{E\delta\left({R_c}^2 - {R_b}^2\right)\left({R_b}^2 - {R_a}^2\right)}{2{R_b}^2\left({R_c}^2 - {R_a}^2\right)} \tag{15}$$

The housing assembly features an outer diameter of 120 mm, with the sleeve component possessing an inner diameter of 50 mm and outer diameter of 77 mm. Under conditions of elevated bearing stress, the interference fit magnitude demonstrating optimal fatigue performance has been established at approximately 1.8% of nominal diameter (Hu et al., 2022). For the current investigation, an interference value (δ) of 0.05 mm was implemented. The material pairing of 42CrMo exhibits a static friction coefficient (μ) of 0.1 and elastic modulus (E) of 206 GPa. The requisite frictional force (F_f) at the sleeve-housing interface may be achieved through precise adjustment of the interference length (h). The functional dependence between h and F_f, as derived from Eq (9), is presented graphically in Fig. 21.

F_f exhibits a linear positive correlation with h. To maintain the frictional force within the specified range (11,297–14,041 N), the interference fit length should be 8.5–10.5 mm. Considering sleeve stability within the housing, the maximum length of 10.5 mm was selected for the interference fit segment.

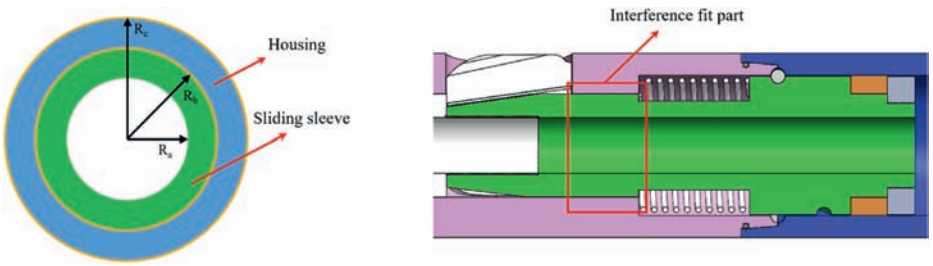


Fig. 20. Interference fit assembly between sliding sleeve and housing.

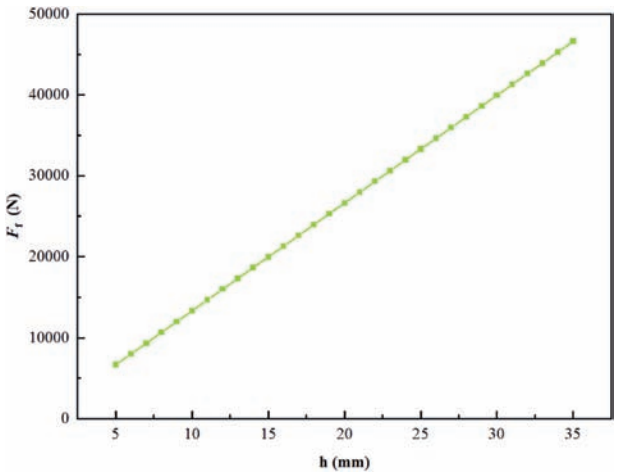


Fig. 21. Relationship between h and F_f.

4. Prototype laboratory testing and performance evaluation

4.1. Procedures for laboratory experiments

The laboratory experiments were conducted to evaluate the operational performance of the reamer prototype, verifying the theoretical analysis framework. Based on a conventional drilling flow rate of 2 L/s and an activation flow rate of 4 L/s for the tool, a prototype was fabricated according to the experimental wellbore dimensions. The wellbore configuration featured 150 mm (ID)/ 170 mm (OD) dimensions, with the drilling reamer and drill pipe assembly having a 90 mm OD. The left and right housing IDs measured 50 mm and 72 mm respectively, while the sleeve parameters (30 mm ID and 6.8 mm interference length) were determined via the previously established equations. The transparent acrylic housing provides both mechanical resilience and optical accessibility for observing locking ball movement trajectories, while the sliding sleeve and arms were manufactured via high-precision 3D printing. The upper annular pressure chamber

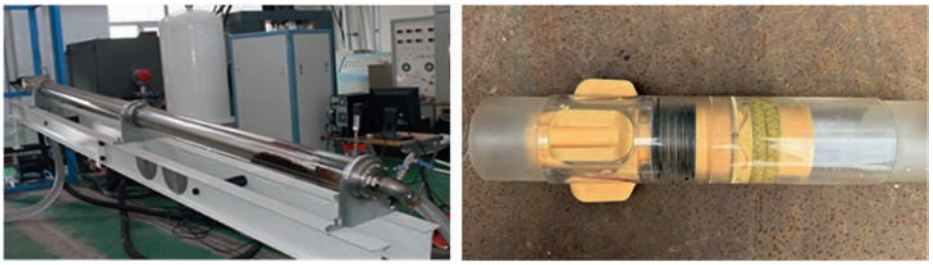


Fig. 22. Experimental setup for the reamer prototype.

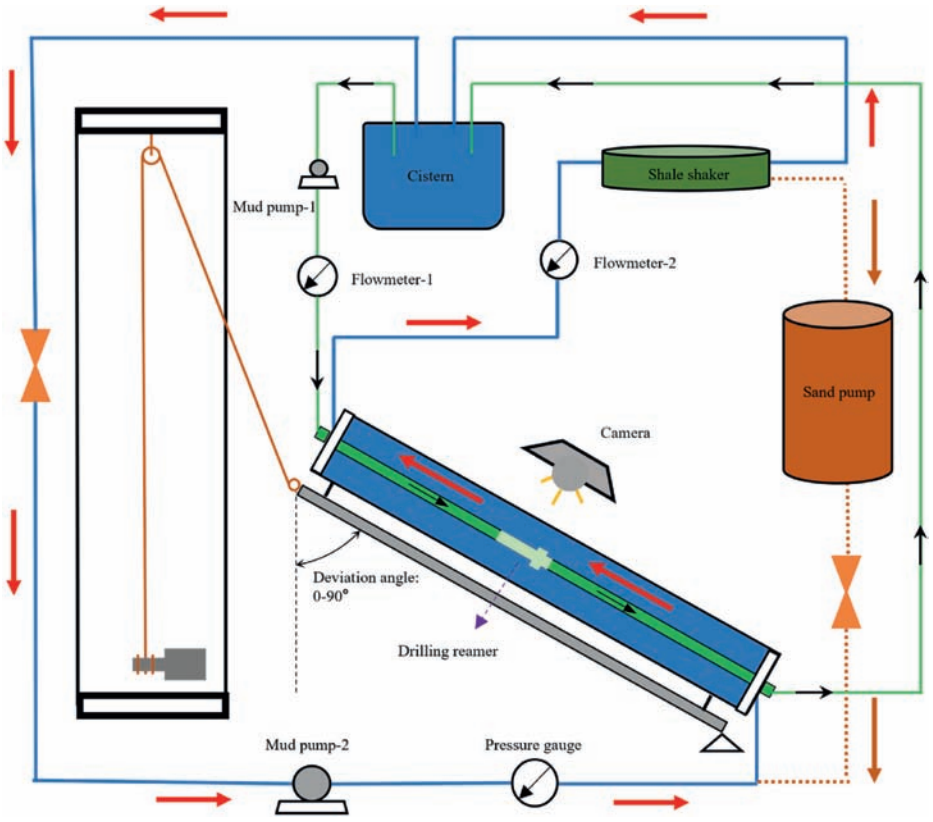


Fig. 23. Schematic of experimental procedure.

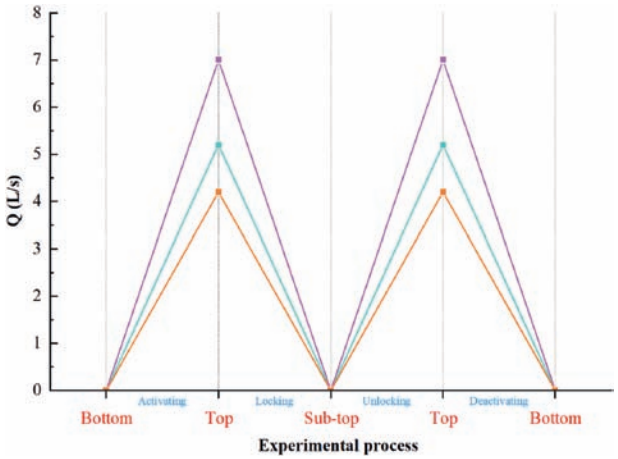


Fig. 24. Relationship between drilling fluid flow rate and operational status.

of the sleeve was sealed using packing elements. The experimental setup for the reamer prototype is shown in Fig. 22.

The horizontal test rig was employed to simulate sidetracking operations, with the reamer prototype installed in the experimental wellbore. A sand-laden drilling fluid (20% sand concentration) was circulated through the annulus to replicate downhole arms conditions, while a high-speed camera system (1000 fps) recorded the tool's dynamic response. As illustrated in Fig. 23, the experimental protocol consisted of the following steps:

(1) Sealing integrity test: Mud pump-2 was activated first, followed by the sand pump and mud pump-1 after flow stabilization. The flow rate was increased to 2 L/s to monitor potential leakage at the packing element.
(2) Arm activation test: While maintaining the flow rate of mud pump-2, mud pump-1 was incrementally ramped up (0.2 L/s steps) until arm deployment. The critical activation flow rate and ball movement trajectory were documented.
(3) Locking mechanism verification: After complete arm deployment, the mud pump-1 was shut down to examine final ball position within the W-shaped track and locking status of arms.
(4) Unlocking performance test: The flow rate was increased again to determine minimum disengagement flow rate and pressure fluctuations during unlocking.
(5) Reset Function Evaluation: Mud pump-1 shutdown and pressure relief, verify the spring reset condition, ball positioning, and complete retraction status of the cutter arms.

4.2. Experimental results and performance analysis

Comprehensive cyclic testing (activation-locking-unlocking-reset) systematically documented the correlation between drilling fluid flow rate and arm deployment status (Fig. 24), confirming the theoretical model's accuracy. High-speed imaging (Fig. 25) captured four characteristic phases of ball movement: standby position (Bottom), dynamic extension (Top), mechanical lock (Sub-top), and reset termination (Bottom).

(1) The reamer maintained structural integrity at the standard 2 L/s drilling flow rate without premature activation, with packing elements demonstrating effective sealing performance throughout the 120-min endurance test.
(2) When progressively increasing mud pump-1's flow rate to 4.2 L/s, the sleeve exhibited a downward displacement of 35 ± 0.5 mm, achieving 35% design compression of the return spring. This precisely positioned the ball at the W-shaped track sub-top, initiating arm deployment within 1.8 s.
(3) Following mud pump-1 shutdown and pressure relief, the return spring drove the sleeve upward through 10% of its stroke, positioning the ball stably at the sub-top of the W-shaped track while the arms achieved complete mechanical locking.
(4) During secondary flow rate increase, the system demonstrated consistent unlocking characteristics at 4.2 ± 0.15 L/s, with the spring compressing 10% of its stroke while the ball reached the top of the W-shaped track.
(5) After final pressure relief, the ball returned to the bottom of the W-shaped track within 2 s as the spring reset the sleeve, resulting in full arm retraction.

Repeated tests demonstrated only a 5% deviation (<0.25 L/s) between the actual activation flow rate and theoretical predictions, confirming the accuracy of the hydro-mechanical coupling model. The tool exhibited reliable performance at the threshold flow rate of 4.2 L/s, with both the locking and reset systems meeting the operational requirements for multiple cycles.

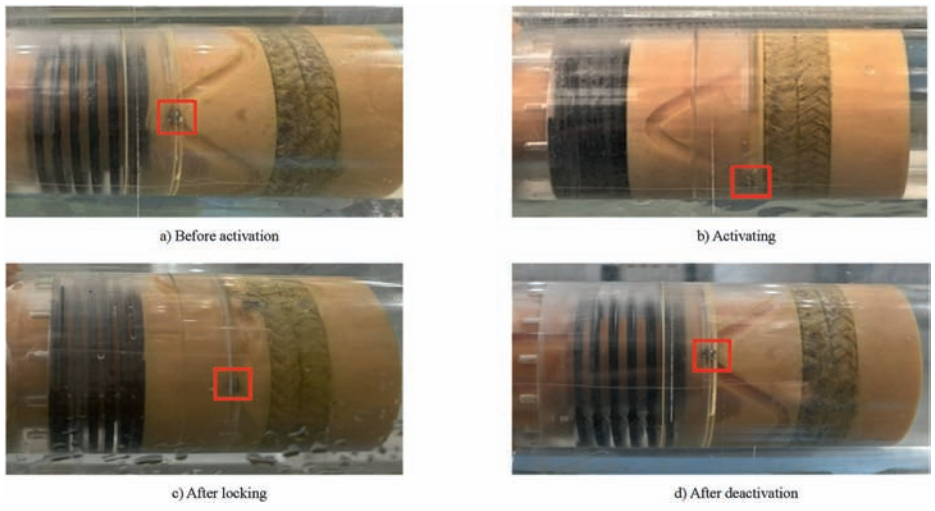


Fig. 25. Trajectory of the locking ball during reamer activation/deactivation cycles.

5. Conclusions

This study presents a systematic investigation of the micro hydraulic reamer-while-drilling (RWD) tool's operational performance through integrated theoretical analysis, structural design, numerical simulation, and laboratory prototype testing. The principal conclusions are as follows:

(1) Mechanical testing of the reamer arms demonstrated that axial stress correlates proportionally with cutting arc angle, while cutting resistance exhibits an inverse relationship. Optimization at a 35° cutting arc effectively reduces resistance while maintaining locking ball stress within elastic limits, preventing plastic deformation that could impede arms activation/retraction.
(2) The line-line contact configuration between the locking ball, housing, and sliding sleeve maintains all component stresses and strains within allowable thresholds. This design prevents plastic deformation in both the ball and contact surfaces, ensuring reliable locking function throughout operational cycles.
(3) Fluid dynamics theory established the sleeve inner diameter design criteria, enabling determination of optimal dimensions based on field drilling parameters. This methodology balances pressure differential requirements with minimized energy loss through precise relationships between flow velocity, pressure differential, and total head loss.
(4) Elastic analysis of thick-walled cylinders yielded a computational model for determining the sleeve-housing interference length. Incorporating field parameters, this model guarantees both prevention of premature activation and positive retraction capability.
(5) Laboratory tests confirmed the prototype's performance, with reamer arms consistently activating at theoretical flow rates and fully retracting upon pump shutdown, validating the design methodology's accuracy (deviation <5%).

The research results provide a theoretical basis for the design optimization and engineering application of micro hydraulic RWD tool.

CRediT authorship contribution statement

Xiaofeng Sun: Writing – review & editing, Funding acquisition, Formal analysis, Conceptualization. **Zuhai Qin:** Writing – review & editing, Writing – original draft, Visualization, Validation, Supervision, Software, Resources, Project administration, Methodology, Investigation, Formal analysis. **Wenhao Wang:** Writing – original draft, Visualization, Validation, Supervision, Software, Resources, Project administration, Methodology, Investigation, Conceptualization. **Tie Yan:** Methodology, Investigation, Conceptualization.

Funding

This work was supported by the National Natural Science Foundation of China (52374007) and the Hainan Province Science and Technology Special Fund (ZDYF2022SHFZ063).

Declaration of competing interest

The authors declare that they have no known competing financial interests or personal relationships that could have appeared to influence the work reported in this paper.

References

Al-Essa, A., 2015. Digital reamer enhances drilling efficiency, economics, and safety. J. Pet. Technol. 67, 38–41. https://doi.org/10.2118/0515-0038-jpt.
Doshvarpassand, S., Richard, T., Mostofi, M., 2017. Effect of groove geometry and cutting edge in rock cutting. J. Pet. Sci. Eng. 151, 1–12. https://doi.org/10.1016/j.petrol.2017.01.023.
Fu, Z., Tergeist, M., Kueck, A., Ostermeyer, G.P., 2022. Investigation of the cutting force response to a PDC cutter in rock using the discrete element method. J. Pet. Sci. Eng. 213, 110330. https://doi.org/10.1016/j.petrol.2022.110330.
Hu, J., Mi, S., Yang, Z., Wang, C., Yang, Y., Tian, W., 2022. An experimental investigation on bearing behavior and failure mechanism of bolted composite interference-fit joints under thermal effects. Eng. Fail. Anal. 131, 105830. https://doi.org/10.1016/j.engfailanal.2021.105830.
Ismayilov, E., Mahmudov, G., 2024. Optimizing drilling operations with slimhole sidetracking techniques: challenges and solutions. In: SPE Casp. Tech. Conf. Exhib. CTC, vol 2024, pp. 1–9. https://doi.org/10.2118/223423-MS.
Koulidis, A., Zhan, G., Ahmed, S., 2022. Embedded force sensing at the cutter. In: ADIPEC 2022. https://doi.org/10.2118/211511-MS.
Lei, Q., Weng, D., Luo, J., Zhang, J., Li, Y., Wang, X., Guan, B., 2019. Achievements and future work of oil and gas production engineering of CNPC. Pet. Explor. Dev. 46, 145–152. https://doi.org/10.1016/S1876-3804(19)30014-X.
Li, S., Li, C., Chen, Z., Zhai, W., Chen, X., Cao, J., 2023. Numerical simulation inversion of creep laws of composite salt layers based on reaming while drilling. Front. Earth Sci. 11, 1–18. https://doi.org/10.3389/feart.2023.1138688.
Liu, C., Song, X., Xu, X., Zong, H., 2022. Adaptability Analysis of Ultra-short Radius. Springer Nature, Singapore. https://doi.org/10.1007/978-981-19-2149-0.
Loreto, J., Zukiwsky, B., Bassiouny, A., Okorie, O.M., 2022. Case study: hitting the bullseye: the evolution of RSS and LWD technology in horizontal Wells. J. Pet. Technol. 74, 38–41. https://doi.org/10.2118/1222-0038-jpt.
Mancini, S., Hitchcock, G., Opsahl, J., Servaes, L., 2009. Drill string vibration mitigation during simultaneous drilling and hole enlargement. In: SPE/IADC Drill. Conf. Proc., vol. 1, pp. 219–226. https://doi.org/10.2118/119260-ms.
Morel, B., Hafle, M., Thomson, I., Ubaru, C., Radford, S., 2010. Proper bit and underreamer synchronization concept delivered excellent performance in GoM deepwater well. In: Proc. Annu. In: Offshore Technol. Conf., vol. 4, pp. 3299–3315. https://doi.org/10.4043/21026-ms.
Murillo, R., Santarini, F., Hurtado, P., Costa, R., Diaz, M.A., 2018. New-generation underreamers reduce trips, decrease operating time, and eliminate nonproductive time. In: Offshore Technol. Conf. Asia 2018. https://doi.org/10.4043/28492-ms.
Noviasta, B., Awaliyah, S., Sonny, S., Pratama, K., Hasibuan, F., 2017. First successful single-trip hole-enlargement-while-drilling and rathole elimination operation in Indonesia using integrated borehole assembly design and modeling. In: SPE Abu Dhabi Int. Pet. Exhib. Conf. 2017. https://doi.org/10.2118/188607-ms.
Rostamsowlat, I., Richard, T., Evans, B., 2018. An experimental study of the effect of back rake angle in rock cutting. Int. J. Rock Mech. Min. Sci. 107, 224–232. https://doi.org/10.1016/j.ijrmms.2018.04.046.
Shokry, A., Elgibaly, A., Salem, A., 2021. Implementation of a novel eccentric dog leg reamer in oil well drilling. J. Pet. Explor. Prod. 11, 1199–1209. https://doi.org/10.1007/s13202-021-01096-3.
Snider, P., Fraley, K., 2007. Marathon, partners adapt RFID technology for downhole drilling, completion applications. Drill. Contract. J 40–41.
State Administration for Market Regulation (SAMR), National Standardization Administration (NSA), 2015. Alloy Structure Steels: GB/T 3077-2015. Standards Press of China, Beijing.
State Administration for Market Regulation (SAMR), National Standardization Administration (NSA), 2016. High-Carbon Chromium Bearing Steel: GB/T 18254-2016. Standards Press of China, Beijing.
Toczek, P., Wisniowski, R., 2024. Enhancing deposit exploitation efficiency utilizing small-diameter radial boreholes via hydraulic drilling nozzles for optimal resource recovery. Appl. Sci. 14. https://doi.org/10.3390/app14093552.
Toczek, P., Wisniowski, R., Zlotkowski, A., Teper, W., 2023. Hydraulic radial drilling using a rotary hydraulic nozzle aimed at increasing the exploitation of deposits. Energies 16. https://doi.org/10.3390/en16237867.
Torvestad, B.T., Ray, T., Hu, J., Gjertsen, O.J., Muir, M., 2012. Development of a new advanced multiple activation system for concentric underreamers. In: SPE/IADC Drill. Conf. Proc., vol. 2, pp. 756–761. https://doi.org/10.2118/151337-ms.
Valverde, E., 2018. Intelligent near-bit reamer affords same-trip drilling, hole enlargement and rathole reduction for optimal deepwater well construction. In: Offshore Technol. Conf. Asia 2018. https://doi.org/10.4043/28402-ms.
Vila, P., Dhaher, K.S., Miller, G., Machado, M., Strachan, P., Nelson, G., Compton, M., Davis, P., Wu, S., 2011. Successful hole enlargement while drilling: deepwater Brazil. In: Proc. Annu. Offshore Technol. Conf., vol. 2, pp. 1019–1029. https://doi.org/10.4043/22637-MS.
Weng, D., Sun, Q., Liang, H., Lei, Q., Guan, B., Mu, L., Liu, H., Zhang, S., Chai, L., Huang, R., 2025. Flexible sidetracking stimulation technology of horizontal wells in low-permeability mature oilfields. Shiyou Kantan Yu Kaifa/Petroleum Explor. Dev. 52, 194–203. https://doi.org/10.11698/PED.20240335.
Yuan, Y., Qi, Z., Yan, W., Zhang, J., Chen, C., 2020. Old well sidetracking selection standards: sulige low-permeability gas field, China. J. Pet. Explor. Prod. Technol. 10, 1699–1709. https://doi.org/10.1007/s13202-019-00827-x.
Zhang, H., Yan, X., Rao, L., Jiang, W., Yan, J., Cui, W., Sun, Y., 2024. Radial multibranch sidetracking technology for low permeability carbonate reservoir

stimulation. In: Soc. Pet. Eng. ADIPEC, pp. 1–9. https://doi.org/10.2118/222060-MS, 2024.
Zhang, J., Wang, G., He, K., Ye, C., 2019. Practice and understanding of sidetracking horizontal drilling in old Wells in sulige gas field, NW China. Pet. Explor. Dev. 46, 384–392. https://doi.org/10.1016/S1876-3804(19)60018-2.
Zhao, J., Liao, H., 2021. Design simulation and test of hydraulic control system of RFID reamer while drilling. In: IOP Conf. Ser. Earth Environ. Sci., vol. 631. https://doi.org/10.1088/1755-1315/631/1/012065.
Zheng, X., Shi, J., Cao, G., Yang, N., Cui, M., Jia, D., Liu, H., 2022. Progress and prospects of oil and gas production engineering technology in China. Pet. Explor. Dev. 49, 644–659. https://doi.org/10.1016/S1876-3804(22)60054-5.
Zhu, X., Zhou, W., Lei, Y., Jia, P., Xue, S., Zhou, B., Xia, Y., 2023. A nonlinear dynamic model for characterizing the downhole motions of the sidetracking tool in a multilateral well. Energies 16. https://doi.org/10.3390/en16020588.